Institute of Atmospheric Sciences, South Dakota School of Mines and Technology, Rapid City, South Dakota, U.S.A.

A Comparison of 3D Model Results with Observations for an Isolated CCOPE Thunderstorm

R. D. Farley, S. Wang, and H. D. Orville

With 17 Figures

Summary

This paper is concerned with the simulation of deep convection for the CCOPE 19 July 1981 case study. Clark's three-dimensional (3D) cloud model modified to use the bulk water parameterization scheme of Lin et al. has been used in the simulation of the CCOPE 19 July 1981 case in coarse mesh, fine mesh, and interactive grid nested schemes, respectively. Comparisons with observations show this 3D grid nested cloud model is capable of both capturing both the dynamic and microphysical properties of the cloud.

In the nested grid fine mesh model simulation, the timing and mode of cloud growth, the diameter of liquid cloud, the cloud top rate of rise, the maximum cloud water content, and the altitude of first radar echo are consistent with observations. The simulated thunderstorm begins to dissipate after precipitation reaches the ground as indicated by the decreasing values of maximum updraft and maximum liquid cloud water content, and ends as a precipitating anvil as was observed in the actual thunderstorm. The model precipitation developed through ice phase processes consistent with the analysis of observations from the actual thunderstorm.

Qualitative comparisons of the actual radar RHIs with simulated reflectively patterns from the 3D model show remarkable similarity, especially after the mature stage is reached. Features of the actual RHI patterns, such as the weak echo region, upshear anvil bulge, strong upwind reflectivity gradients, and the upwind outflow region near the surface are reproduced in the simulation. Comparison of the actual radar PPIs with horizontal cross sections of radar reflectivity simulated by the 3D model, however, show modest differences in the storm size with the 3D simulated thunderstorm being 1–2 km longer in the west-east direction than the actual thunderstorm. The model-predicted maximum updraft speed is smaller than the 2D model-predicted maximum updraft speed, but still greater than what was observed.

Comparisons among the nested grid fine mesh model (MB), nested grid coarse mesh model (MA), fine mesh model (FM), coarse mesh model (CM), and 2D model results previously published show that the nested grid fine mesh model (MB) gives the best simulation result. The various 3D model simulation results are generally similar to each other except for the difference in the domain maximum values. The domain maximum values in the fine mesh models (MB and FM) are generally higher than the coarse mesh models as a result of averaging over a smaller area.

1. Introduction and Background

Clouds are tremendously complex dynamic systems. Due to their large scale and their complexity, detailed measurements of every aspect of a cloud or a laboratory produced cloud are impossible as the standard means for exploring clouds. Therefore, numerical simulation is necessary for a better understanding of the physical characteristics and dynamics of a cloud.

However, the limitations of present computer capability impose severe constraints on cloud modeling, especially on three-dimensional (3D) cloud modeling. As a result, all cloud processes cannot be included in detail and simplifications must be made. It is important to determine whether convection can realistically be simulated in spite of the simplifications applied in cloud models.

Since the realistic simulation of convection is a prerequisite for the application of cloud models in important areas like cumulus transport and the prediction of the amount and distribution of precipitation, the verification of 3D cloud models against observations is necessary and desirable.

Over the past two decades, many 3D simulations have been presented; only a few of these many studies are mentioned in the following brief review. The general practice of verifying cumulus models has been the comparison of some of the numerical results against typical magnitudes of observed variables in convective clouds. Steiner (1973), Cotton and Tripoli (1978), and Schlesinger (1978) found general agreement in liquid water content and cloud circulations between simulated results and those obtained from observations made in a number of clouds. Miller (1978) and Clark (1979) focused their attention on the comparison with multicellular storms (they studied different storms). Although qualitative agreement was found in rainfall patterns, cloud water content, and updraft structures, quantitative discrepancies did exist, particularly in storm duration (Miller, 1978) and storm propagation speed (Clark, 1979). Smolarkiewicz and Clark (1985) simulated a field of clouds for a particular day from the 1981 CCOPE project and found close agreement between observations and model results in the global characteristics of the cloud field structure, type of clouds, sky cloud coverage, and time evolution of the whole field. Redelsperger and Lafore (1988) simulated a tropical squall line. Their simulation exhibited the circulation pattern characteristic of a squall line and reached an intensity in agreement with observations after they included the forcing induced by the rear inflow jet.

In a different type of comparison, Schlesinger (1984) compared 2D and 3D model storm simulations and concluded that the updraft in the 2D storm is much weaker than the updraft in the 3D storm. Orville (1985) disputed these conclusions and criticized Schlesinger for such sweeping conclusions based on only two cases.

The present paper is concerned with a 3D cloud model simulation of deep convection for the CCOPE 19 July 1981 case study. This CCOPE case has also been simulated using an electrified version of the IAS two-dimensional, time-dependent model by Helsdon and Farley (1987a, b). Some of the results of that study are summarized in this paper. A brief description of the Clark three-dimensional cloud model as applied in this study is presented in section 2, followed by a summary of the CCOPE 19 July 1981 observational results in section 3. In section 4, a detailed comparison of model results and observations combined with discussion is presented. Finally, a summary is presented in section 5.

2. Brief Description of the Model

2.1 Overview

The three-dimensional cloud model has been developed by Clark and associates (Clark, 1977, 1979, 1982; Clark and Farley, 1984). The model uses the deep anelastic equations of Ogura and Phillips (1962). Sub-grid scale turbulence is parameterized according to the first-order theory of Smagorinsky (1963) and Lilly (1962). The eddy mixing coefficients are functions of the flow field and the local Richardson number, so that both wind shear and thermal stability determine the magnitude of the coefficients. Open (radiation) boundary conditions are used at the side boundaries.

Clark's 3D model originally employed bulk water microphysics similar to Kessler (1969) for cloud water and rain mixing ratios. Recently, Farley has modified this 3D model to use the bulk water parameterization scheme of Lin et al. (1983), plus secondary ice production as described by Aleksić et al. (1989), and graupel/hail fromation via snow (of a certain critical size) accreting supercooled cloud water as explained by Farley et al. (1989). The Lin et al. (1983) microphysical scheme employed in the model is based on concepts suggested by Kessler (1969) and divides water and ice hydrometer into five classes: cloud water, cloud ice, rain, snow, and high density precipitating ice (graupel/hail). These five classes of hydrometeors interact with each other and water vapor through a variety of crude parameterizations of the physical processes of condensation/evaporation, collision/coalescence and collision/aggregation, accretion, freezing, melting, and deposition/sublimation. Rain, snow, and graupel/hail, which are assumed to follow inverse exponential size distributions, possess appreciable terminal fall velocities. Cloud water and cloud ice have zero terminal velocities and thus travel with the air parcels. For a detailed discussion of the microphysical processes

and parameterizations employed in the model, the reader is referred to Wisner et al. (1972), Orville and Kopp (1977), and Lin et al. (1983).

A two-way interactive grid nesting framework has been applied in the model (Clark and Farley, 1984); the grid nesting allows one to focus on desired regions of the domain and obtain higher spatial resolution with greater computational efficiency. The grid nesting is accomplished by running several models in parallel in an interactive sense. The same program code is used for each model by simply "switching" the implied dimensions and other relevant variables at the beginning of a model's time integration. Further discussion and the basic equations are given in the above citations.

2.2 Numerical Approximations and Boundary Conditions

2.2.1 Numerical Approximations

This three-dimensional cloud model is a finite difference model. The equations in the model are approximated in flux conservative form on the staggered-grid mesh of Harlow and Welch (1965), also known as the Arakawa C-grid. The model dynamics are solved using the second-order quadratically conservative scheme of Arakawa (1966) and Lilly (1965) for the spatial derivative terms, and a second-order leapfrog scheme for the time tendency terms. The newly added water substance and other scalar fields are treated with a modified upstream differencing scheme advocated by Smolarkiewicz (1984) and Smolarkiewicz and Clark (1986).

2.2.2 Inner Model Boundary Conditions

Figure 1 shows a schematic representation of the grid structure for two models using a nesting ratio 2:1. The inner nested model derives its boundary conditions from the solution of the outer model. Four dynamic terms are required for solution of momentum equations at each of the six boundary planes of the inner model. For example, at $x = x_0$, we need $\bar{\rho}^x u$ at $t = (\tau + 1) \Delta t$, and $\overline{\bar{\rho}^x u^x \bar{u}^x}$, v, and ω at $x = x_0 - \Delta x/2$, $t = \tau \Delta t$. Here the Shuman type linear operator

$$\bar{\phi}^\eta = \frac{1}{2}\left[\phi\left(\eta + \frac{\Delta\eta}{2}\right) + \phi\left(\eta - \frac{\Delta\eta}{2}\right)\right]$$

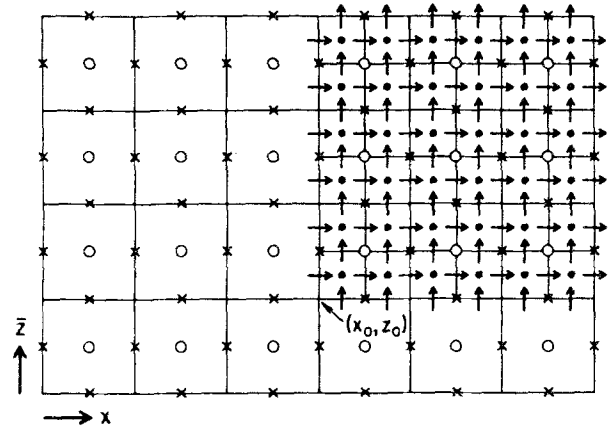for the arbitrary variable ϕ and dimension η was

Fig. 1. A two-dimensional schematic of the staggered grid structure for two models with two-to-one nesting ratio. The circles mark the CM model positions of θ, ρ, and P, and the crosses mark the velocity component positions. Dots mark the FM model scalar variables, and arrows mark the velocity component positions. [From Clark and Farley, 1984]

used. In treating the mixing terms at the inner model boundaries, the normal derivative of the eddy coefficient is taken to be zero. Scalar quantities such as θ or moisture are obtained by extrapolation from the coarser model; in the case of scalars, only the value at $x = x_0 - \Delta x/2$ type boundaries need be specified.

2.2.3 Outermost Model Boundary Conditions

For the outermost model, the boundary conditions on the velocity components (u, v, ω) and potential temperature θ at the upper and lower boundaries are taken as

$$\omega = \frac{\partial}{\partial z}(\bar{\rho}^x u) = \frac{\partial}{\partial z}(\bar{\rho}^x v) = \frac{\partial^2 \theta}{\partial z^2} = 0 \text{ at } z = 0, H. \quad (1)$$

Here we have assumed zero normal velocity gradient conditions. The condition on θ and other scalars in (1) is actually applied at $z = + \Delta z/2$; $H - \Delta z/2$. Equation (1) is used primarily for the advection terms, Coriolis terms and buoyancy terms, and to provide a local structure to u and v at $z = 0$. Because (1) becomes inconsistent with momentum exchange between the surface and near surface air as $\Delta z \rightarrow 0$, the surface stress is treated by a drag law formulation such that

$$\begin{cases} \tau_{13} = \frac{1}{2}\rho CD|V_t|(i \cdot V_t) \\ \tau_{23} = \frac{1}{2}\rho CD|V_t|(j \cdot V_t) \end{cases} \text{ at } z = 0. \quad (2)$$

In (2), CD is drag coefficient, V_t the horizontal

velocity vector tangent to the surface [which from (1) is equivalent to the velocity at $z = \Delta z/2$], ρ is the air density, and i, j are unit vectors in the x and y directions, respectively. At $z = H$, both τ_{13} and τ_{23} are put equal to zero.

The surface sensible heat flux is specified either as zero or, as in Clark and Gall (1982), to non-zero values dependent upon the incident solar short-wave flux.

Near the model top, a region of Rayleigh friction is employed to absorb vertically-propagating gravity waves. Grid nesting is avoided in regions of the absorber.

The lateral boundary conditions are treated using a combination of specification and extrapolation. At outflow boundaries, the normal velocity component is calculated using the extrapolation procedure of Orlanski (1976). All other field values are obtained by taking one-sided "averages" of the advection equations. At inflow boundaries, the normal velocity is treated by a combination of the Orlanski scheme and time relaxation to environmental values, as in Clark (1979, 1982), Clark and Gall (1982), and Kurihara and Bender (1983). All other field values are set equal to their respective environmental values at the inflow boundaries.

2.2.4 Grid Nesting Considerations

An important consideration for application of grid nesting is the reversibility of the averaging and interpolation formula. In other words, the inter-polation formula used to derive the boundary conditions from the coarse mesh (CM) for use in a fine mesh (FM) model must be consistent with the operators used to average the FM data back to the CM resolution. For details of the treatment, the reader is referred to Clark and Farley (1984).

3. Summary of the Observations

The cloud in question for the following discussion was observed during the CCOPE project on 19 July 1981. On that day, the microphysical and electrical life cycle of an isolated cumulus congestus was investigated using four powered aircraft, an instrumented sailplane, and two meteorological radars with Doppler capability. The observations commenced very early in the life of the cloud when the radar reflectivity was below the detection limit of -5 dBz. The measurements continued for 40 min, through the period of active growth during which

the storm grew into a small electrified cumulo-nimbus with radar reflectivity up to 55 dBz, and then into the dissipating stage when only a precip-itation trail remained. The results of the NCAR sailplane ascent were first presented by Jones et al. (1982), and the preliminary analyses of the Desert Research Institute Aerocommander data were discussed by Gardiner et al. (1985). More recently, Dye et al. (1986) have presented a comprehensive synthesis and analysis of the majority of the data pertinent to the investigation of the 19 July storm, to which the reader is referred for details. These analyses have led to the char-acterization of the cloud and its evolutionary history. It also should be noted that this cloud was a study case for both International Cloud Modeling Workshops in 1985 and 1988, respectively, (WMO, 1986, 1988). A brief summary made by Helsdon and Farley (1987a) will be quoted at this point for convenience.

'The cloud was found to exhibit a single-cell life cycle, growing in a moderately unstable environ-ment that was characterized by weak wind shear. It underwent a rapid growth phase after the cloud top reached the $-22\,°C$ level. Cloud base was at 3.8 km above mean sea level (MSL) ($+1\,°C$) and the cloud top reached a height of about 10.5 km ($-48\,°C$). The liquid cloud was between 6 and 8 km in its maximum horizontal dimensions at all levels and had an adiabatic core (with liquid water contents reaching $2.75\,\mathrm{g\,m}^{-3}$) up to at least 7 km. The in-cloud $0\,°C$ isotherm was found to be at 4 km in the updraft core. Updrafts at cloud base were between 1 and $5\,\mathrm{m\,s}^{-1}$, and the in-cloud values during the strong growth phase ranged from 10 to $15\,\mathrm{m\,s}^{-1}$. Doppler analysis showed a convergent layer in the lower half of the cloud which ascended and increased in depth with time until dissipation began, at which time the con-vergence began to disappear. On the basis of hydrometer measurements, which showed that the only identifiable liquid particles were cloud droplets with diameters typically less than $20\,\mu m$, it has been inferred that the formation of precipitation took place through ice processes. This has been found to be typical of cumulus clouds of this type in the High Plains."

Many of the observational features were captured in the two-dimensional (2D) simulation reported in Helsdon and Farley (1987a, b). One impetus for the application of the 3D model to

this case was to see how well the 3D model could do in similar comparisons and what additional comparisons could be made with the observations. In the comparisons which follow, all 2D results cited are from Helsdon and Farley (1987a).

4. Results and Discussions

4.1 Description of the 3D Model Experiments

The modified form of Clark's 3D cloud model described in section 2 has been tested under three different grid meshes. First, the model was run with a coarse mesh, the grid interval being 800 meters in both x and y directions and 500 meters in the z direction; hereafter we will refer to the coarse mesh test as CM. Second, the model was run with a fine mesh, using grid intervals of 400 meters in both x and y directions and 250 meters in the z direction; hereafter we will refer to the fine mesh test as FM. Third, a nested model calculation was executed with the fine mesh version and the coarse mesh version run simultaneously,

Table 1. Basic Information on the Numerical Experiments

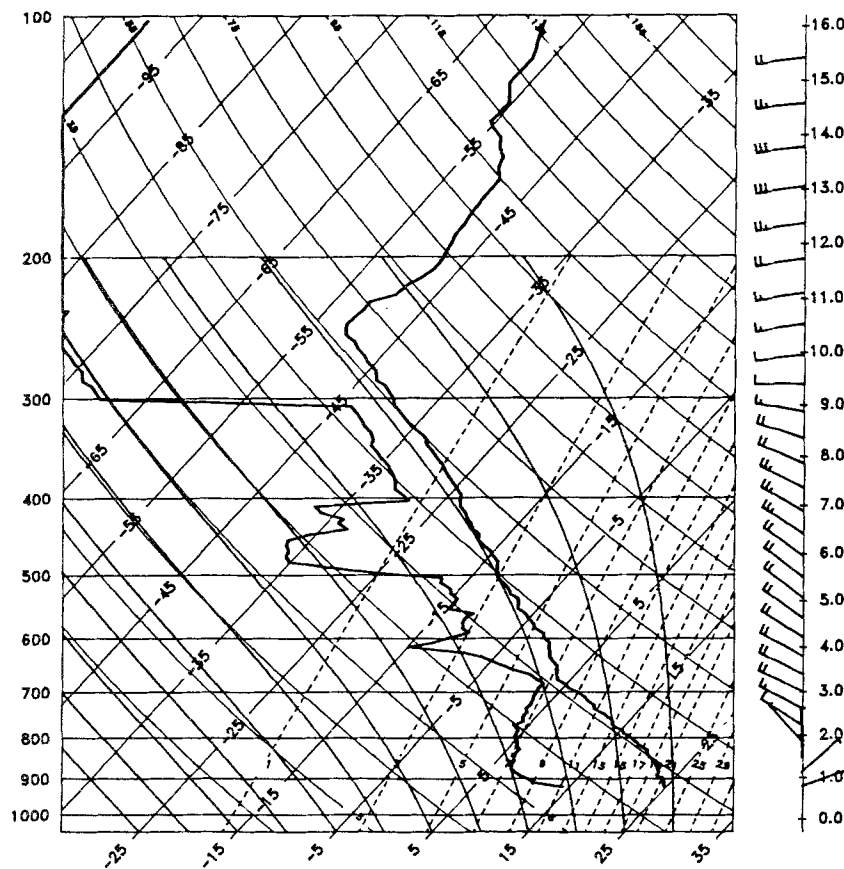| Experiment	Domain (km)	NX, NY, NZ	$\Delta x, \Delta y, \Delta z$ (m)	Δt (sec)
2D	19.2×19.2	97, 97	200, 200	variable
3D/CM	$40 \times 40 \times 20$	52, 52, 42	800, 800, 500	6
3D/FM	$20 \times 20 \times 15$	52, 52, 62	400, 400, 250	6
3D/MA*	$40 \times 40 \times 20$	52, 52, 42	800, 800, 500	6
3D/MB*	$20 \times 20 \times 10$	52, 52, 42	400, 400, 250	6

* Interactive case.

Fig. 2. The 1440 MDT Miles City, Montana, sounding for 19 July 1981

interacting with each other; hereafter we will refer to the fine mesh interactive results as MB and the coarse mesh interactive results as MA. [Note that both of these results come from the same run.] Table 1 provides some basic information about the cases discussed in this section.

The base state of the atmosphere for these model runs is taken from the 1440 MDT sounding at Miles City, Montana, on 19 July 1981. This sounding of temperature and moisture, shown in Fig. 2, represents the atmosphere approximately

1.5 hours prior to the formation of the observed cloud and was taken approximately 35 km to the east of the initial cumulonimbus development area. The input sounding for the 3D model runs (Fig. 3) is modified from the original sounding to make the cloud base in closer agreement with what was observed. The Galilean transformation applied to allow for grid translation assumes storm motion from 300° at $9\,\mathrm{m\,s^{-1}}$.

The development of the clouds in all 3D model runs were triggered by perturbations of the envi-
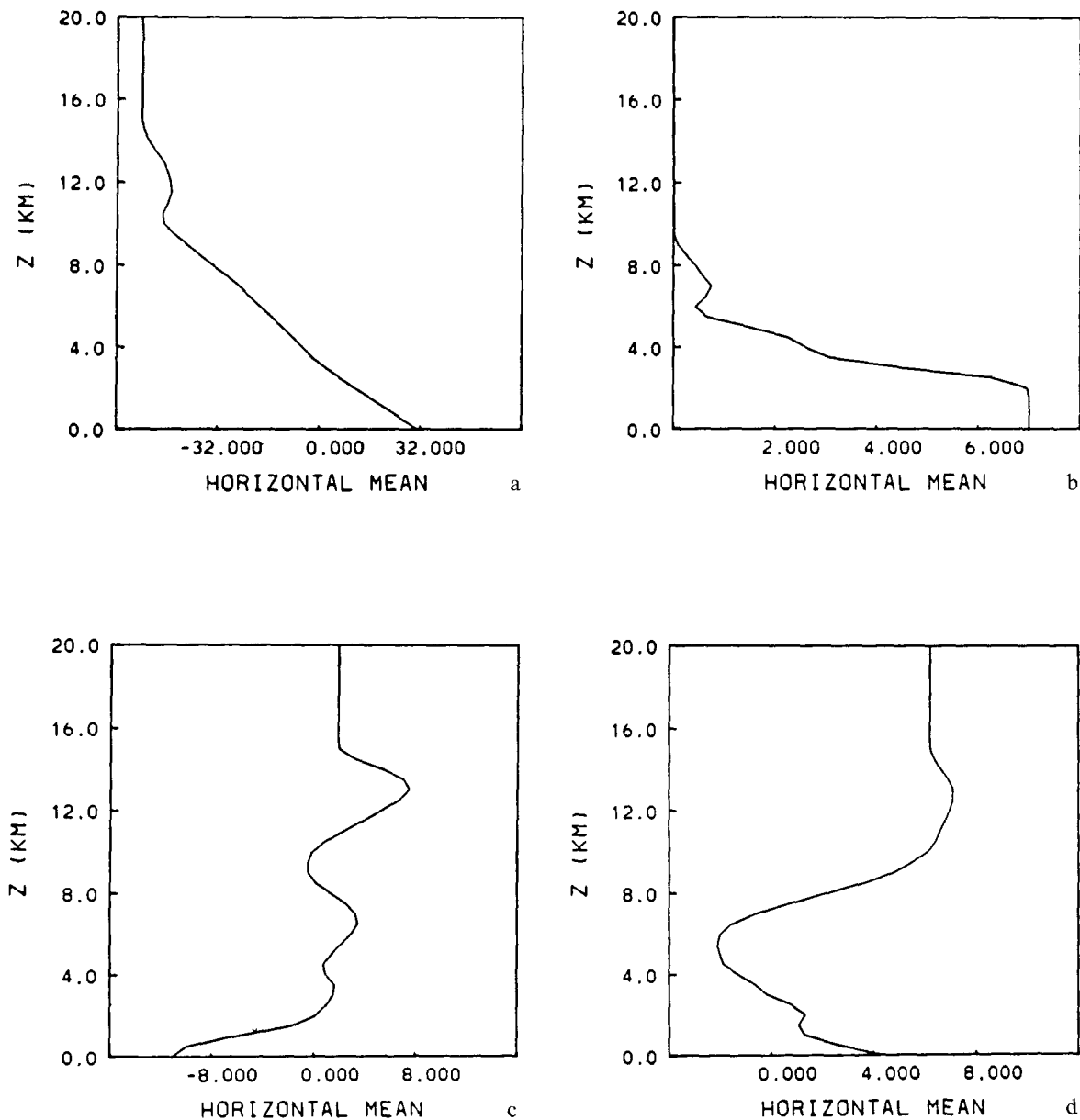
Fig. 3. Model input environmental conditions for the 19 July 1981 CCOPE case: (a) temperature; (b) water vapor mixing ratio; (c) and (d) the x and y components of the wind velocity, respectively. The sounding (Fig. 2) was modified to agree with observed cloud-base temperature and pressure

ronmental temperature and humidity at time zero in these models. The warm moist bubble had a combination of a 2 °C maximum amplitude in temperature and a 5% maximum increase in water vapor, and was placed in the horizontal center of each model domain. This bubble was in the shape of a sphere with a radius of 3 km and was centered at 3.5 km above the ground. The amplitude of the perturbations decreased in proportion to the square of the distance away from the center of the bubble.

4.2 MB Simulation Results and Discussions

4.2.1 Establishment of Reference Time

Since we are trying to make the comparison between model clouds and the observed cloud as detailed as possible, a timing reference must be established. The timing correspondence was based on the comparison of the history of cloud top development for the observed cloud and all 3D model clouds and is presented in Fig. 4 and Table 2. In order to make the model cloud top development close to the observed cloud top development, the model time of 0 min is set equivalent to Mountain Daylight Time (MDT) 1610. Helsdon and Farley (1987a) developed a similar timing reference based on the beginning of a rapid growth phase; this rapid growth phase was quite distinct from the earlier period of more subdued cloud growth and was consistent with the discussion in section 3. In
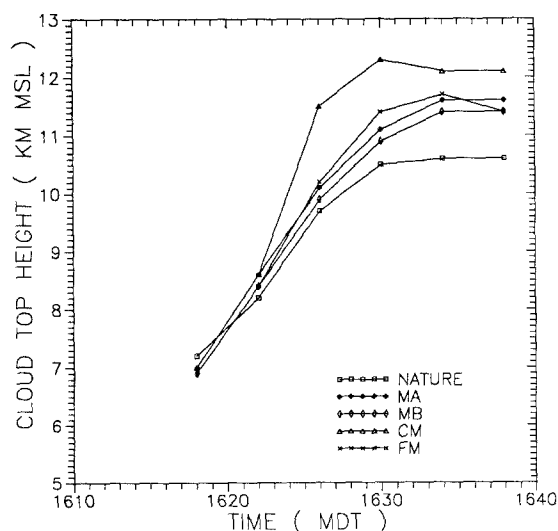

Fig. 4. Cloud top height versus time for the observed cloud and all 3D model clouds

Table 2. *Cloud Top Development*

| Time (min) | Cloud top height (km) | | | | |
	Nature	MA	MB	CM	FM
8–1618	7.2	7.0	6.9	7.0	6.9
12–1622	8.2	8.6	8.4	8.6	8.4
16–1626	9.7	10.1	9.9	11.5	10.2
20–1630	10.5	11.1	10.9*	12.3	11.4
24–1634	10.6	11.6	11.4*	12.1	11.7
28–1638	10.6	11.6	11.4*	12.1	11.4

* This is an estimated value.

the 3D model cases, the cloud grows quite rapidly, but a distinct rapid growth phase is not readily discernible because the earlier cloud growth was not markedly subdued as in nature and the 2D simulation.

4.2.2 General Appearance

In the following three subsections, the 3D model results are presented, with special emphasis given to the nested grid fine mesh cloud model experiment (MB).

The cloud life cycle is depicted in Fig. 5, which shows 3D perspectives of the simulated cloud at 4 min intervals starting at 4 min simulation time (1614 MDT). The perspectives were produced by plotting the surface of the combined cloud water and cloud ice field at $q_{cw} + q_{ci} = 0.1$ g kg^{-1}. Note that the top of the cloud extends beyond the MB model top at 20 min. The results from MA for the time period 20–40 min are shown in Fig. 6. A much more detailed cloud appearance and evolution are depicted in Fig. 7, which displays simulated west-east vertical cross sections of the cloud including precipitation and storm-relative wind vectors for case MB. Information concerning the plotting symbols is given in the figure caption.

From Figs. 5 and 7 we see that the simulated cloud is a single cell storm. Initial cloud formation was at 4 min (1614 MDT). The cloud grows quickly and expands its size until 16 min (1626 MDT); then the upper level cloud spread horizontally very quickly. The main fallout of precipitation (graupel and rain) occurs between 24 and 36 min (1634–1646 MDT). By 40 min (1650), the lower level clouds start to disappear and the anvil is the dominant remaining cloud form. The initial precipitation formed was snow, with 0.068 g kg^{-1} indicated
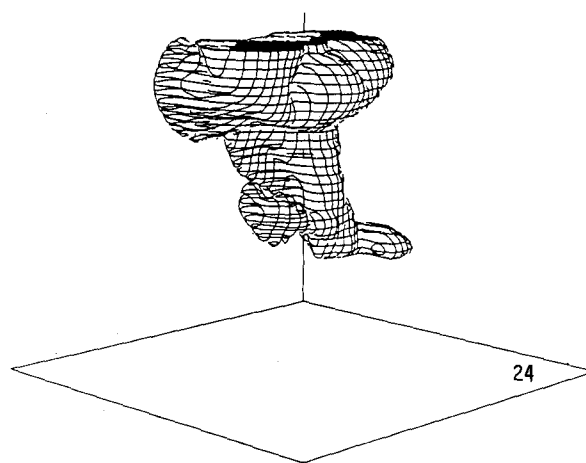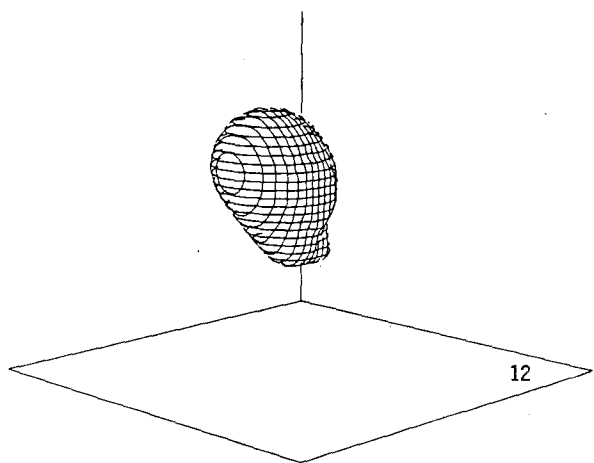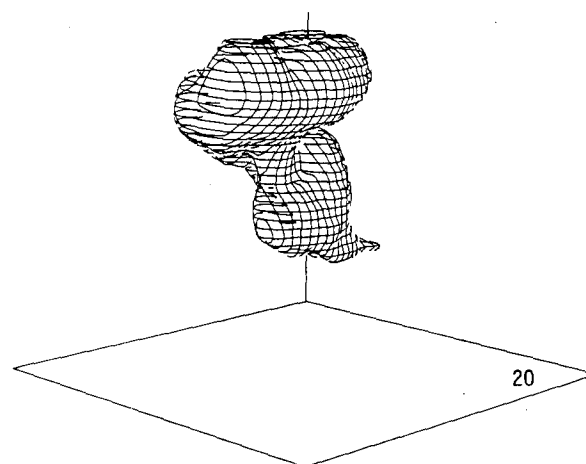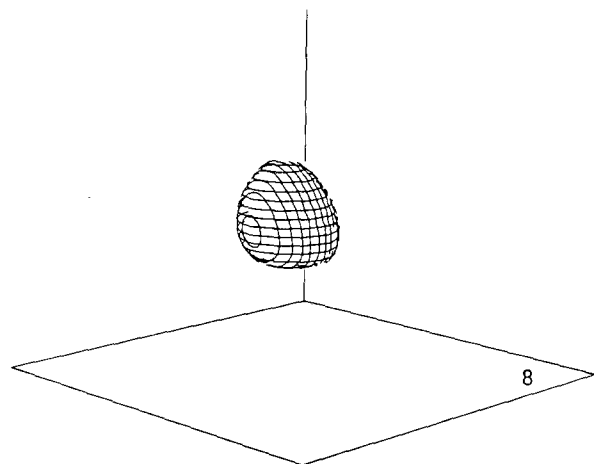
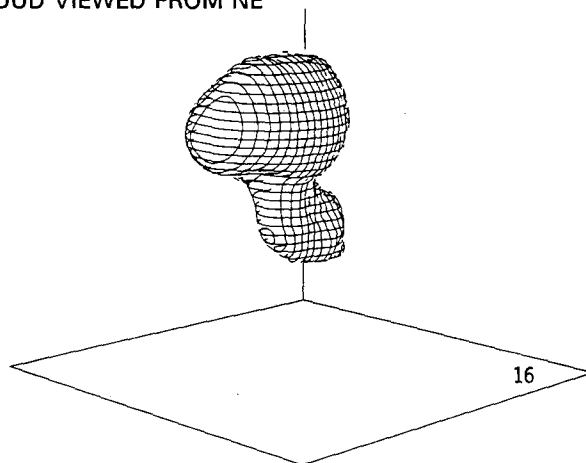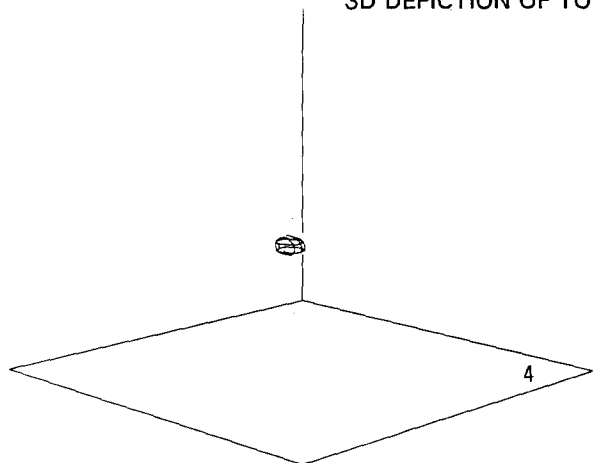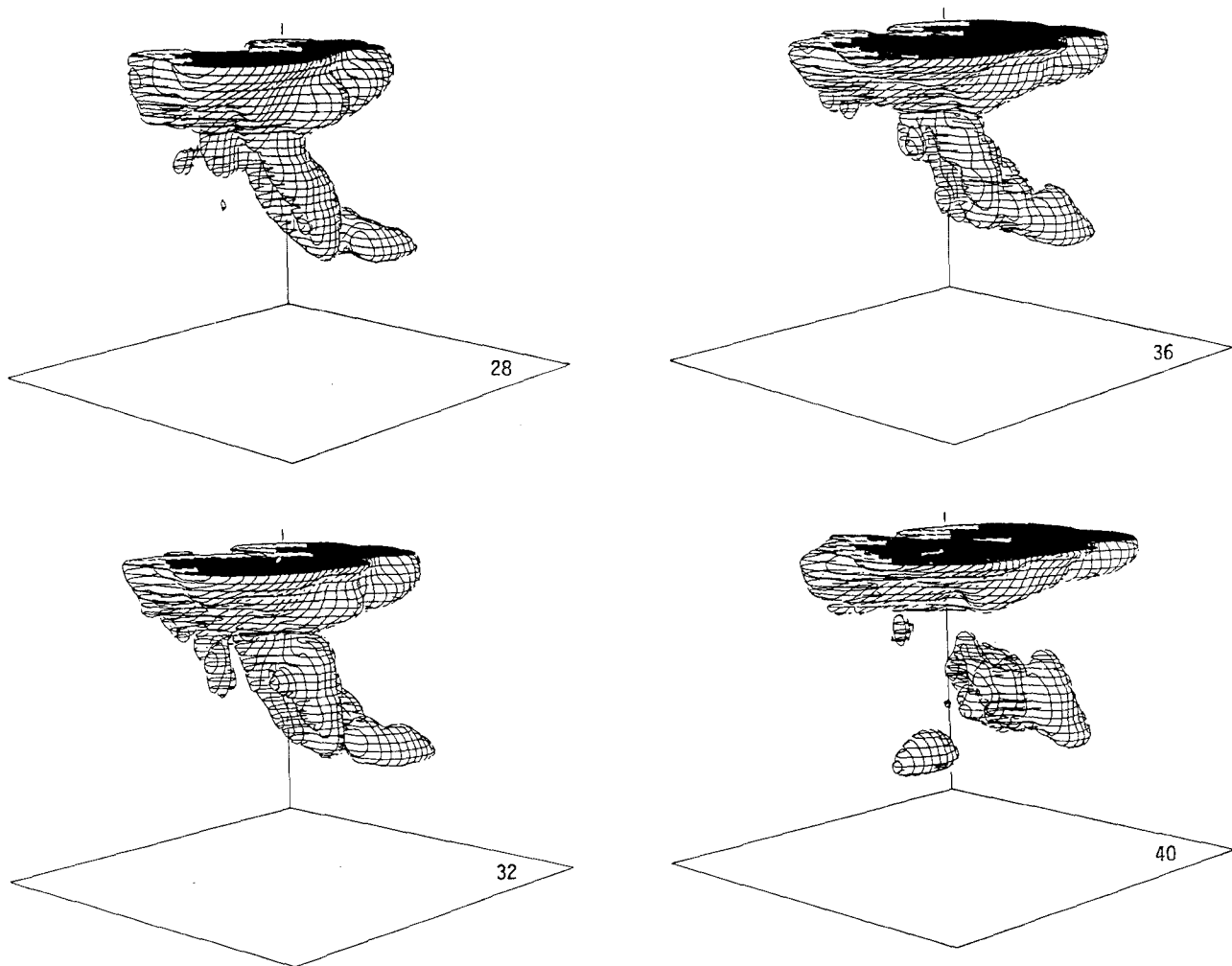3D DEPICTION OF TOTAL CLOUD VIEWED FROM NE

Fig. 5. *Continued*

Fig. 5. The three-dimensional perspectives of the stimulated cloud at 4-min intervals starting at 4 min through 40 min simulation time for case MB. Perspectives are viewed from northeast and do not include precipitation

between 6 and 7 km MSL at 8 min (1618 MDT). At that time, no radar echo was detected, as indicated by observations. Figure 8 shows the initial simulated radar reflectivity in excess of 20 dBz which occurred at 12–1622 with a maximum value of 26 dBz near 7.5 km MSL. The radar echo is associated with the formation of snow because no other precipitation forms were found at that time. The first 5 dBz return occurred just after 10 min (1620) at 7 km (MSL), which is close to the observed first echo height, although it occurred 3 min sooner than observed.

The cloud-base altitude maintains itself at 3.8 km MSL throughout the simulated cloud development in agreement with the observations. Since the domain of MB is not high enough to keep the cloud top in it, the final simulated cloud-top height cannot be detected from MB. For Table 2, we have

predicted the simulated cloud top for MB based on similarities of contours and contour gradients compared to MA and FM, and arrived at an estimate of 11.4 km. Therefore the simulated cloud top is less than 1 km higher than 10.6 km, the observed maximum cloud top height, and 0.4 km higher than the value that one would expect based upon parcel theory applied to the sounding. It should be noted, however, that the available information about the cloud top is not nearly as well documented as the cloud-base height as indicated in Helsdon and Farley (1987a).

The precipitation processes becomes active through an ice phase path. The cloud ice, which first formed around 6–1616, grows and transforms to snow. At 13–1623, graupel/hail has formed through riming of the snow particles and by 16–1626 begins to fall out on the downshear side

R. D. Farley et al.

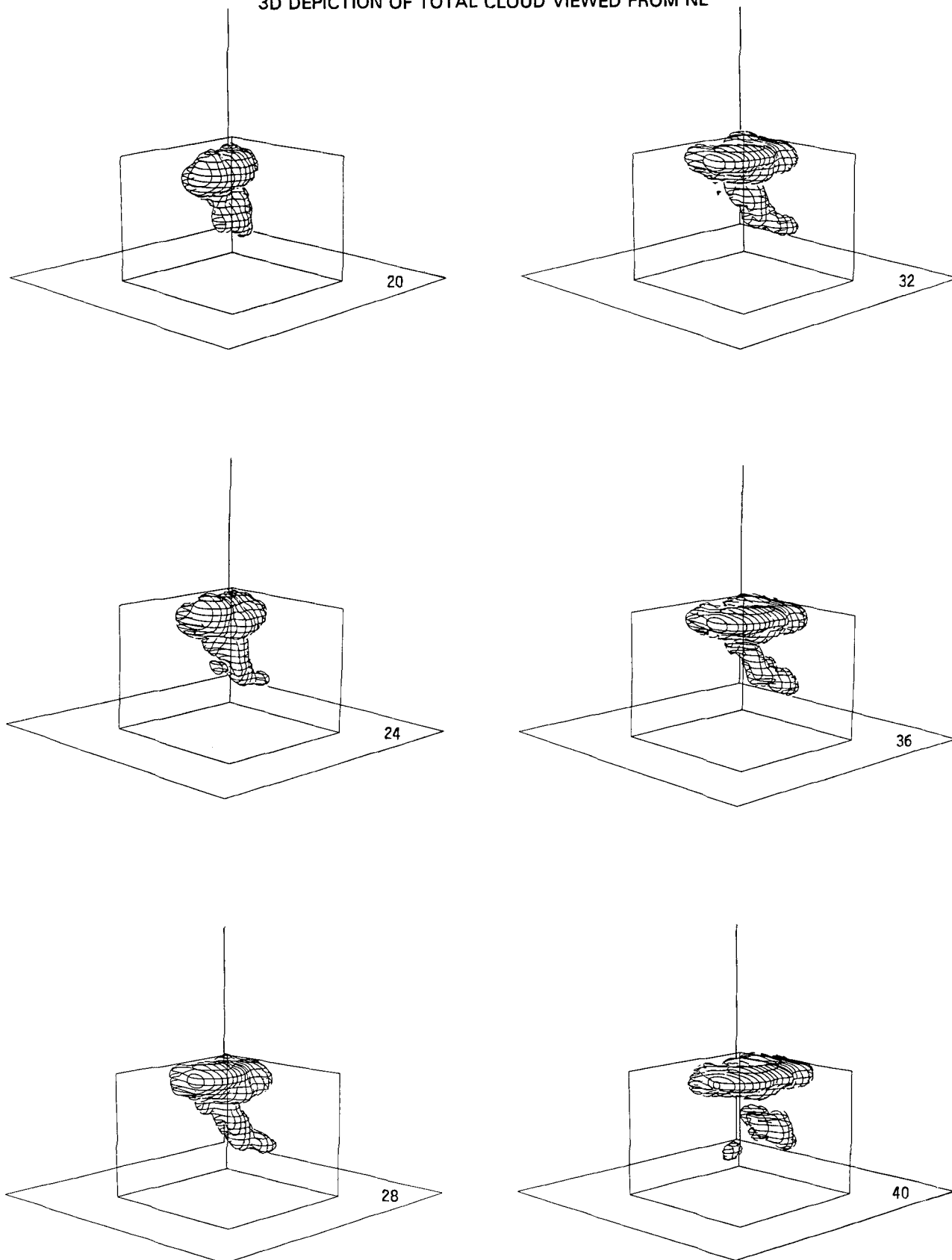## 3D DEPICTION OF TOTAL CLOUD VIEWED FROM NE

Fig. 6. As in Fig. 5, but for case MA for the time period 20 to 40 min simulation time

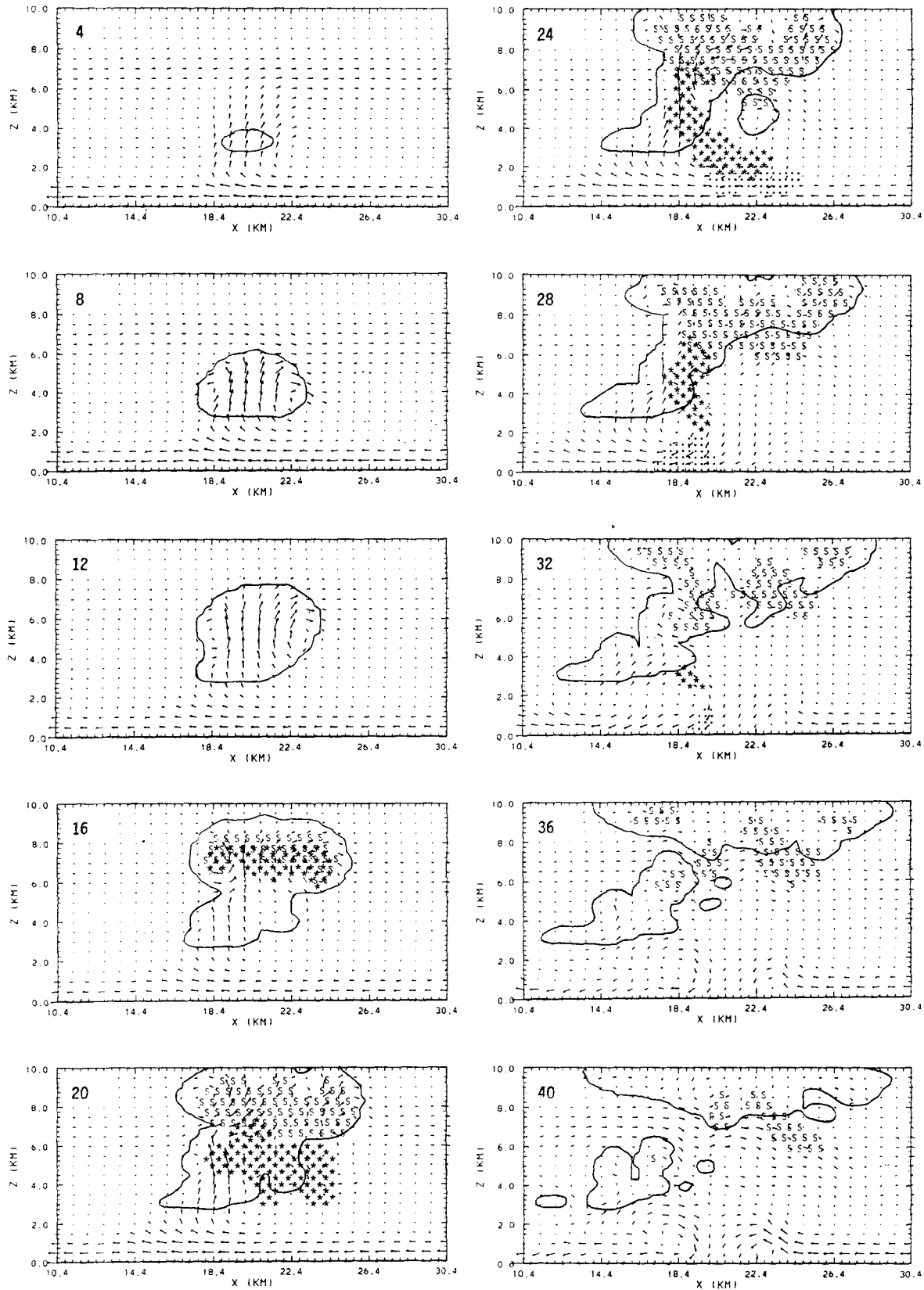## CLOUD AND PRECIPITATION DEPICTION AT Y = 20 KM

Fig. 7. Simulated west-east vertical cross sections of the cloud, including precipitation and storm-relative wind vectors at $Y = 20$ km for case MB. Solid lines indicate cloud outline $(q_{CW} + q_{CI} > 0.01 \, \mathrm{g\,kg^{-1}})$; S, snow $(> 0.5 \, \mathrm{g\,kg^{-1}})$; asterisks, graupel/hail $(> 0.5 \, \mathrm{g\,kg^{-1}})$; and heavy dots, rain $(> 0.5 \, \mathrm{g\,kg^{-1}})$. Times are indicated in the upper left-hand corner of each frame. All heights are above ground level (AGL = MSL − 800 m)
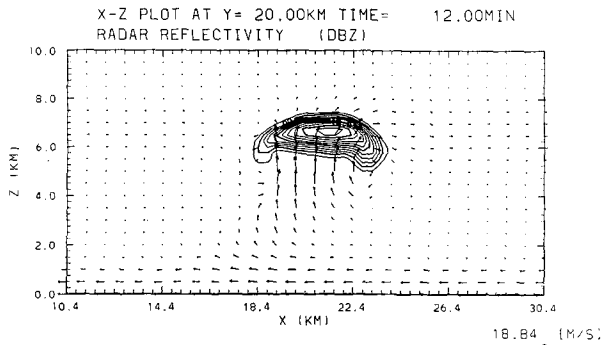
Fig. 8. Simulated west-east vertical cross section of the radar reflectivity for case MB at $Y = 20$ km and time 12-1622. The contour interval is 2 dB and the outer contour is 2 dBz

Fig. 9. Plots of domain maximum cloud water mixing ratios for cases MA and MB in grams per gram, as function of time

of the updraft. As the graupel/hail shower falls below the melting level, near 4.1 km MSL in the environment, melting begins to occur, leading to the formation of rain as indicated at 20-1630. During the period from 24-1634 through 28-1638, we see that the precipitation process acts to erode away the lower portion of the cloud, while the anvil continues to grow and spread downwind.

Another observable which can be determined from examination of Fig. 7 is the lateral extent of the liquid cloud. Dye et al. (1986) report that the maximum visual and radar storm diameter at mid-levels was about 6 km. By examining the cloud dimensions at various times in the region between 4 and 5 km AGL, which is below the ice-dominated anvil region, we see the maximum liquid cloud dimension is about 6 km.

4.2.3 Microphysical and Dynamic Comparisons

Figure 9 shows the temporal evolution of the maximum cloud water mixing ratio for 3D cases MA and MB. The maximum cloud water mixing ratio predicted by the model (MB) is 5.6 g kg^{-1} at an altitude of 8.2 km MSL ($\rho = 0.48$ kg m^{-3}) at 15-1625, which corresponds to a water content of 2.7 g m^{-3}. This high liquid water region occurs just above the maximum updraft in the updraft core, and the height and the value of the maximum decrease thereafter. According to Fig. 7 of Dye et al. (1986), the sailplane encountered its maximum liquid water content (LWC) of 2.5 g m^{-3} at 7 km ($\rho = 0.587$ kg m^{-3}) and 20-1630. This is lower and later than the altitude and time of the model maximum. The model cloud liquid water mixing ratio at a height of 7 km and time 20-1630 is
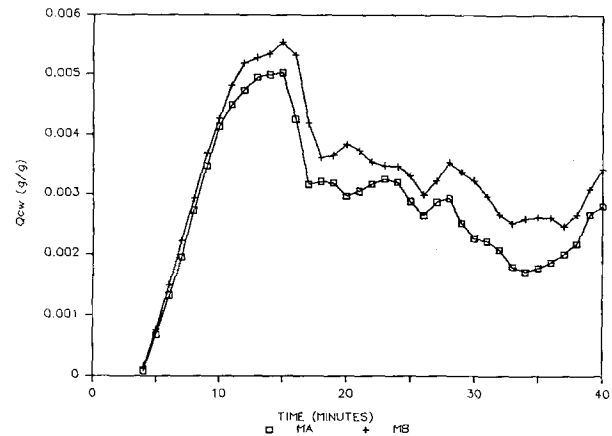
between 2.5 and 3 g kg^{-1} which corresponds to LWCs of 1.47 and 1.76 g m^{-3}, respectively. The maximum liquid cloud water mixing ratio at that time is 3.9 g kg^{-1} (2.33 g m^{-3}), and is 0.6 km lower. By examining the model output, we find that the maximum cloud water content was simulated quite well; however, the modeled cloud grows faster and is dynamically more active than the observed cloud.

Another feature which can be determined from the model output is the drying out of the cloud. The cloud water mixing ratio reaches its maximum at 15-1625, 1 min after the peak updraft speed (Fig. 10). Subsequently, a dramatic decrease in both the maximum cloud liquid water and updraft takes place. Examination of the model output of the cloud water field at 16-1626 (Fig. 11) reveals that the reduction in maximum cloud liquid and the decrease of the updraft at that time are
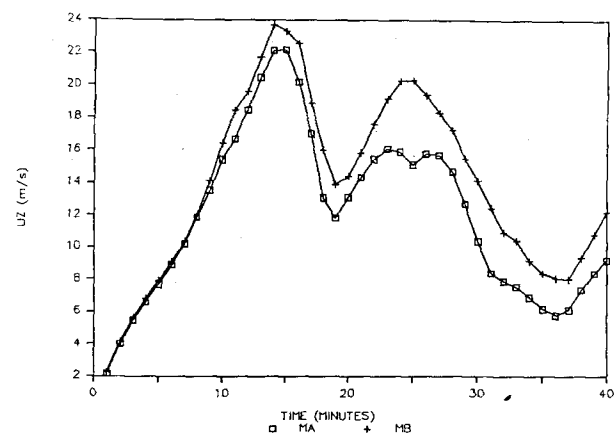

Fig. 10. Plots of domain maximum updraft speed in meters per second as functions of time for cases MA and MB
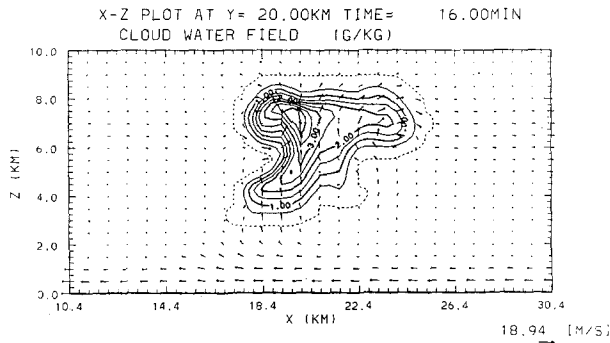
X-Z PLOT AT Y= 20.00KM TIME=   16.00MIN
CLOUD WATER FIELD   (G/KG)

Fig. 11. Model output of west-east vertical cross section of cloud water field for case MB at $Y = 20$ km and at time 16-1626. The contour interval is 0.5 g kg^{-1}. The dashed line indicates the cloud boundary (0.01 g kg^{-1})

X-Z PLOT AT Y= 20.00KM TIME=   16.00MIN
GRAUPEL/HAIL FIELD   (G/KG)

Fig. 13. Simulated west-east vertical cross section of graupel/hail field for case MB at $Y = 20$ km and at 16-1626. The contour interval is 0.125 g/kg

the results of entrainment of ambient air. The maximum cloud water mixing ratio, however, increased slightly again about 18-1628. For our purposes, we determine the time the cloud starts drying out based on the beginning of a sustained decrease in maximum cloud water mixing ratio at mid levels. For MB, this occurs at 22-1632. The comparison of simulated cloud liquid desiccation with observation is quite favourable. Dye et al. (1986) estimated from aircraft data and time lapse photographs that the actual cloud desiccation commenced around 1632.

The first appearance of significant graupel/hail in the simulation is seen in Fig. 12 to occur at 14-1624, The sailplane detected a single 3.6-mm ice particle in the updraft at an altitude of 4.8 at 16-1626. The King Air, operating at 6 km, detected a 1.6-mm image between 1622 and 1623 and a 2.2-mm image on its next pass, between 1625 and 1626. From Fig. 13, which is a vertical cross section
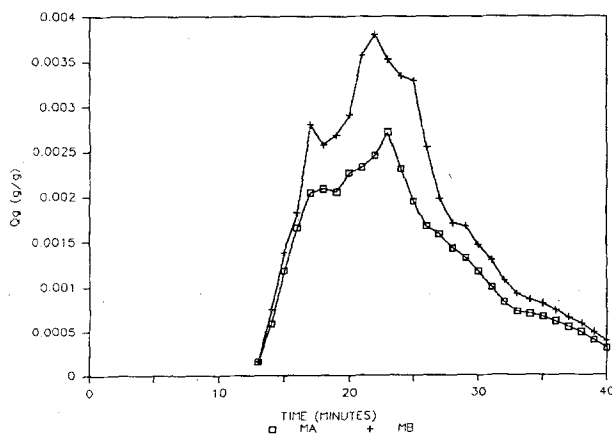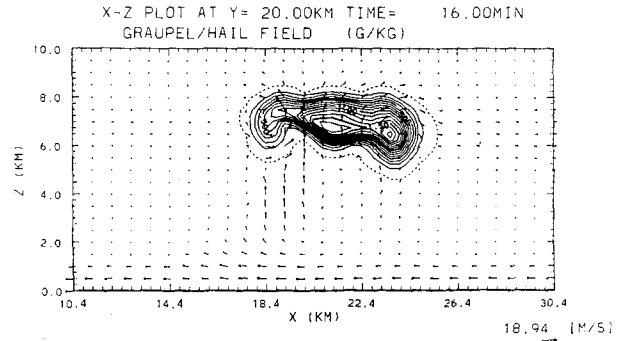
of model predicted graupel/hail mixing ratio at 16-1626, we see that a hypothetical airplane at 16-1626 would likely detect graupel/hail between 5.8 to 6 km MSL and downwind of the main updraft.

Figure 10 shows the evolution of maximum vertical velocity. The vertical velocity rapidly increased to its maximum value in the first 14 minutes of the simulation. The cloud growth rate is very rapid during this time. By 14-1624, the cloud top reached a height of 9 km MSL. A calculation of the cloud top rise rate based on the data in Table 2 leads to values of 3.3-7.1 m s^{-1}, which compares favorably with the 4-7 m s^{-1} calculated from data in Jones et al. (1982).

As explained by Helsdon and Farley (1987a), the comparison of the simulated maximum updraft speed with the observations is not as easy as with some other observables due to the fact that the observable is available only at the time and place where the measurement is being made. The maximum updrafts speed achieved in the model simulation is 23.7 m s^{-1}, which occurs at 14-1624, and an altitude of 7.8 km MSL. The maximum updraft encountered by the various aircraft penetrating the storm are reported to be between 10 and 15 m s^{-1}. To make a better comparison, the model results at a distinct time and altitude are compared against the sailplane measurement, since the sailplane made its ascent in the main updraft of the cloud.

According to Dye et al. (1986), the sailplane found sustained updrafts from 1619 to 1631 with maximum values of 3 to 5 m s^{-1} at cloud base and 10 to 15 m s^{-1} at 6 to 7 km. Near 20-1630 (7 km), updraft speeds at 14 m s^{-1} were recorded. At

Fig. 12. Plots of domain maximum graupel mixing ratios in grams per gram as functions of time for cases MA and MB
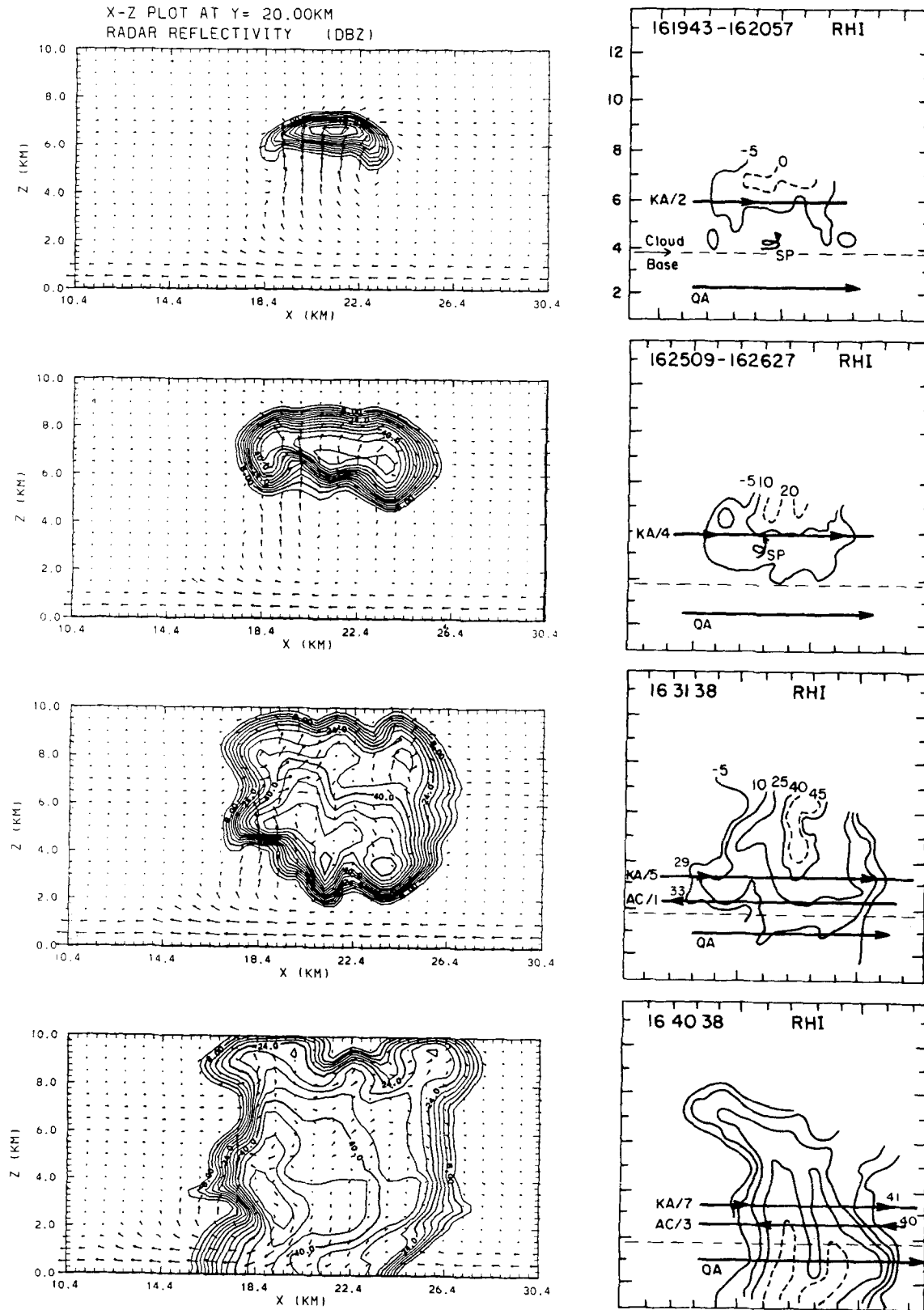
Fig. 14. Comparative plots of model-generated west-east vertical cross section of radar reflectivity at $Y = 20$ km (left panel) and actual CP-2 RHIs (right panel) for case MB. Model plots have 4 dB contour intervals. CP-2 RHIs have 15 dB contour intervals except for the dashed lines, which are labeled. The positions of aircraft are indicated by bold arrows. Tick marks are at every 1 km. The CP-2 RHIs are extracted from Fig. 4 of Dye et al. (1986)

20–1630 in the model simulation, the maximum updraft was $14 \, m \, s^{-1}$ near 5.5 km MSL, which is about 1.5 km below the sailplane altitude. A 1-km cross section through the main portion of the model updraft at 7 km for 16–1626 yields speeds about $16 \, m \, s^{-1}$, which is comparable to those measured. Examining the simulated cloud base updraft shows that the updraft speed near base ranges from 2 to $8 \, m \, s^{-1}$.

Finally, Dye et al. (1986) estimate that the decay of the updraft began around 24–1634 MDT. As can be seen in Fig. 10, the sustained decay of the updraft in the simulation (except for that caused by entrainment as discussed earlier) commences at 25–1635. The decay starts at near the right time but decreases at a slower rate than was observed.

4.2.4 Radar

Figure 14 shows a side-by-side comparison of modeled and observed radar reflectivity profiles at four comparable times. The left-hand column in Fig. 14 contains the model simulated radar reflectivity; the contour interval is 4 dB and the outer contour has a value of 4 dBz. The right-hand column in Fig. 14 contains range-hight indicators (RHIs) extracted from Fig. 4 of Dye et al. (1986). The contour interval is 15 dB except for dashed lines, which are labeled, and the outer contour is − 5 dBz. Figure 14 is presented for qualitative comparisons only because the magnitude of the radar reflectivity factor, as calculated in bulk water simulations, are typically overestimated (Smith et al., 1975).

Looking at the first pair of plots, with the model plot taken at 12–1622, which is about 2 minutes later than the CP-2 RHI data, we note the simulated radar echo and actual CP-2 RHI radar echo bear the same pattern. The altitude of the maximum echoes in the middle of the cloud above the main updraft is higher than the echoes at the sides of the clouds in both model and actual radar echoes.

At 16–1626, we note the strongest echoes are located at the same altitudes, about 7 km MSL, which is associated with the maximum graupel/hail field in the model. Also note that at 16–1626, the altitude of the radar echo in the middle of the cloud is no longer higher than the edges. By examining the model snow and graupel/hail fields (Figs. 13 and 15), we see that the updraft underneath the middle of the cloud is weaker than it is in other
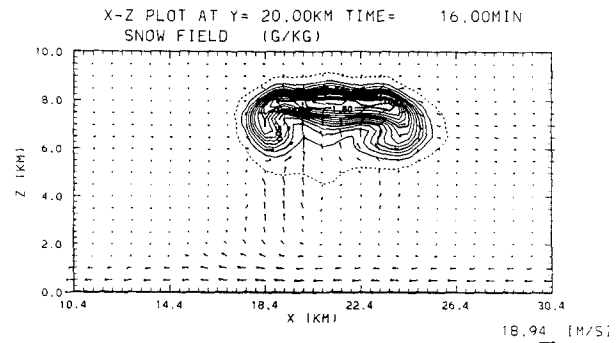

Fig. 15. Simulated west-east vertical cross section of the snow field for case MB at $Y = 10$ km and at 16–1626. Contour interval is 0.125 g/kg

regions, and the boundary of the snow field and boundary of the graupel/hail field show the same patterns as the radar echo.

Looking at the third pair of plots, for which the simulated radar echo is about 2 minutes earlier than the actual CP-2 RHI, we see that there exists a great deal of similarity between the model results and the actual CP-2 RHI, especially the shape of the radar echo outline. A notable exception is the maximum echo region, which is associated with the graupel/hail shower and which is lower in the simulation than in the real cloud, although horizontally its position matches well with respect to other identifiable features. By examining the model output, we see the high level indentation on the left side of the cloud (about 7.5 km MSL) is associated with the ambient air entrainment, and the low level weak-echo region on the left part of the cloud (about 4.8 km MSL) is associated with the inflow feeding the updraft.

Looking at the fourth pair of plots, with the simulated radar echo again about 2 minutes earlier than the actual CP-2 RHI, we see that there are two precipitation shafts in the CP-2 RHI and they seem to be merging as they approach the ground. In the simulation, there is only one precipitation shaft, although it matches the upwind shaft in the RHI. The outflow regions on both sides near the ground are evident in both the simulation and the RHI, as is the anvil. Also the strong reflectivity gradients present near the cloud edge are evident in both panels.

Figure 16 shows a side-by-side comparison of horizontal cross sections of radar reflectivity for the modeled cloud and actual CP-2 PPIs extracted from Fig. 4 of Dye et al. (1986). The contour
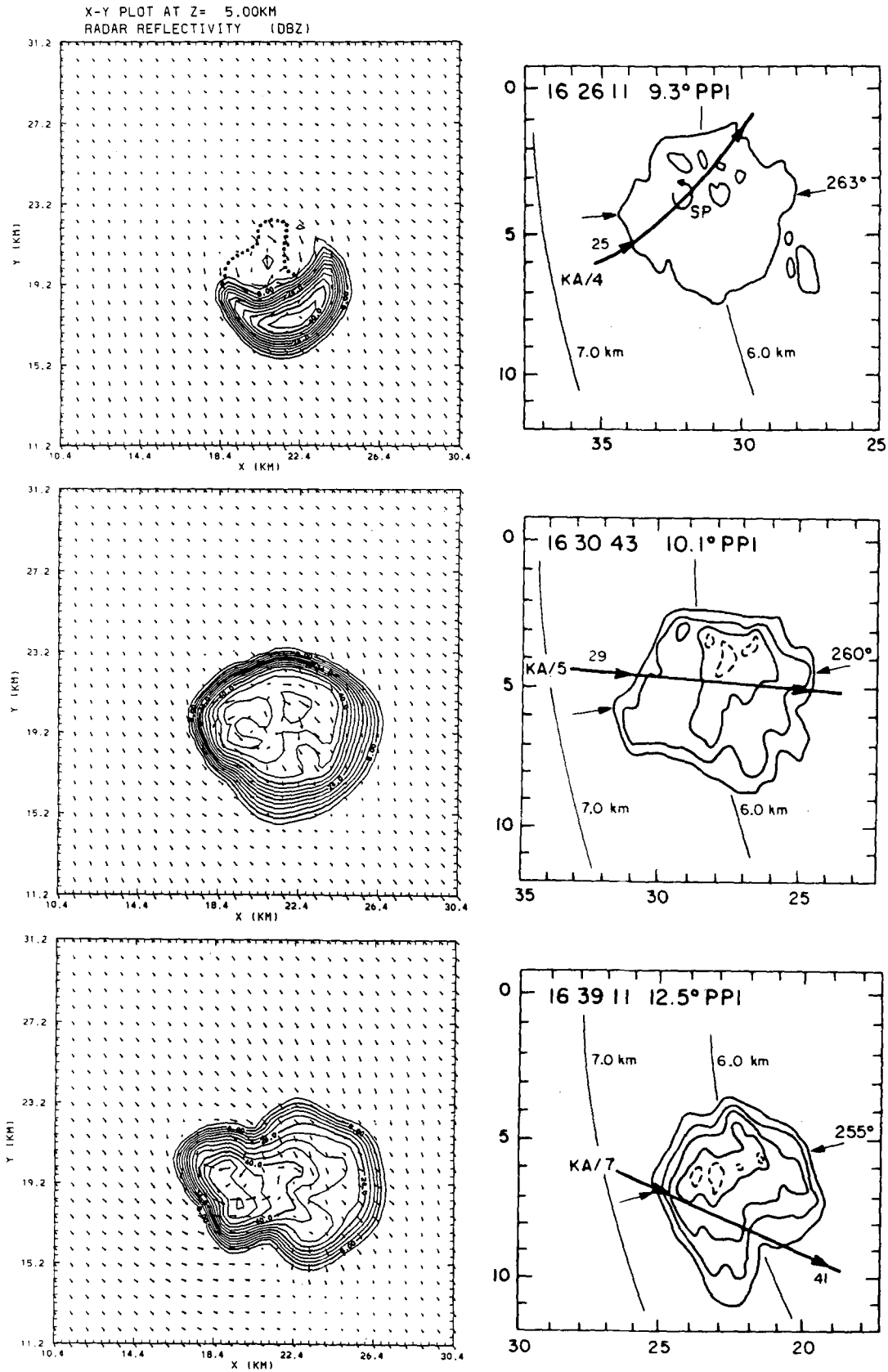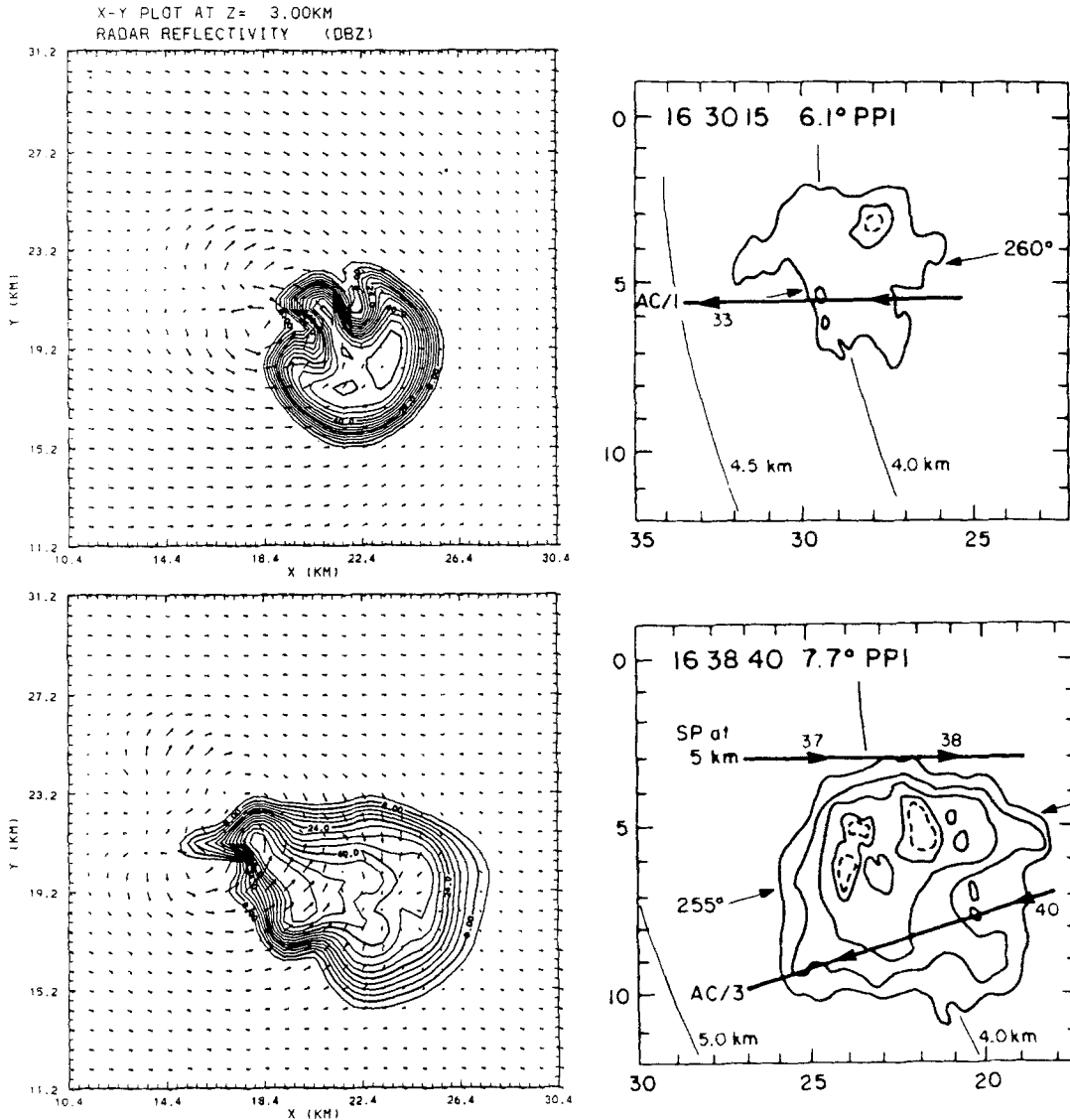
Fig. 16. *Continued*

Fig. 16. Comparative plots of model-generated horizontal cross-sections (left panel) and actual CP-2 PPIs (right panel). Model plots have 4-dB contour intervals. CP-2 PPIs have 15 dB contour intervals except for the dashed lines. Tick marks are at every 1 km. The CP-2 PPIs are extracted from Fig. 4 of Dye et al. (1986)

intervals are the same as used in Fig. 14. For the model cross sections, the first three pairs of plots are taken at 5.8 km MSL, whereas the last two plots are taken at 3.8 km MSL.

The first pair of plots show the radar echo patterns at 16–1626. The heavy dotted line in the model plot is the 0.01 g kg^{-1} contour of the snow field. At this time, the size of the simulated and observed clouds are quite comparable, except the maximum radar reflectivity regions are different. By examining the simulated snow field and graupel/hail field at the same time and altitude, we see that the maximum radar reflectivity region

is associated with the maximum graupel/hail field. Thus the maximum graupel/hail field must have been shifted from what was observed in the early stage.

The second pair of plots show the radar echo patterns at 20–1630. Note that the shape of the two radar echoes are comparable, except the simulated radar echo is elongated in the X-direction, being 1 to 2 km larger than observed.

In the third pair of plots, the simulated radar echo is taken at 28–1638, about 1 min earlier than the time of the observation. Comparison shows that the left part of the simulated radar echo does

not appear in nature. If we ignore the left part of the simulation, then the radar reflectivity comparison is quite good regarding the packing of the isopleths and the storm size.

The last two simulated plots of radar echo are taken at 20–1630 and 28–1638, which are both within 1 min of the observation times. By examining the last two pair of plots, we see that the model simulated radar echoes show "hook" patterns which are not observed in the actual CP-2 PPIs. The storm dimension is comparable in the north-south direction, but larger than what was observed in the west-east direction.

4.3 2D and Other 3D Model Simulation Results

Figure 3, in Helsdon and Farley (1987a), shows the evolution of the cloud for the 2D model simulation. Comparing that figure with Fig. 7, we see that in addition to the lower cloud base height in the 2D model simulation, these model simulated clouds are quite different especially in the early stages. The slow cloud growth characteristics of the early stages in the 2D model simulation are not indicated in any of the 3D model simulations. The appendage which appeared on the upshear side against the environmental flow between 4 and 6 km AGL (1623–1629) in the 2D model simulation does not exist in the 3D simulations. The cloud structures, however, show favorable similarity after 1630. Both simulations indicate the main updraft on the upshear (left) side of the cloud

and the precipitation fallout occurring on the downshear (right) side. There is an erosion of cloud below 6 km AGL on the downshear side during the mature phase, and both simulations indicate anvil extending downshear. The timing of the fallout of precipitation and the character of the precipitation are also quite similar during the mature phase.

Table 3 shows an overall quantitative comparison among the various 3D cases, the 2D simulation, and the observations. From this table, we can see that the fine mesh interactive 3D model simulation (MB) is better than the 2D model simulation and the other 3D cases in a number of respects. The simulation of cloud base height and maximum liquid cloud water content have been improved significantly. Additional discussion and results for these cases are given in a thesis by Wang (1989).

Since there are many differences between the 2D and 3D models as indicated in this paper and Helsdon and Farley (1987a), the difference in geometry in the two models should not be considered as the only cause of the differences between 2D model results and 3D model results. Slight differences in microphysics and numerics, differences in initial conditions, both wind and thermodynamics, spatial resolution, and grid structure are prime reasons for different results.

A final note regarding the comparison between 3D cases MB and FM illustrates another aspect and advantage of grid nesting. Figure 17 shows

Table 3. *Quantitative Comparisons Among the 3D Cases (MA, MB, CM, FM), the 2D Case* (Helsdon and Farley, 1987a) *and the Observations*

Feature	MA	MB	CM	FM	2D	Observations
Cloud base height (km)	3.55	3.8	3.55	3.8	2.8	3.8
Maximum cloud top height (km)	11.6	11.4*	12.3	11.7	11.6	10.6
Cloud top rise rate (m s^{-1})	3–7	3–7	4–12	3–7	3–8	5–7
Liquid cloud size at mid-levels (km)	6	6	6	6	6	6
Maximum liquid water content (g m^{-3})	1.82	2.33	2.12	2.30	4.08	2.50
at 1630 and height (km)	6.3	6.4	6.3	6.8	6.2	7.0
Time liquid cloud drying out begins	1632	1632	1628	1630	1630	1632
Time of first graupel	1624	1624	1624	1624	1625	1626
Maximum vertical velocity (m s^{-1})	22.0	23.7	21.8	25.0	26.0	10–15
Time updraft decay begins	1636	1638	1634	1636	1632	1634
Cloud base updraft (m s^{-1})	2–8	3–10	2–7	2–8	1–7	1–5
Time of first 5 dBz radar echo and height	1620	1620	1621*	1620	1620–1623	1623
	6.8	7.0	7.1*	6.8	7.0	7.0

* Estimated values.

X-Z PLOT AT Y= 10.00KM TIME= 40.00MIN
TOTAL CLOUD FIELD (G/KG)

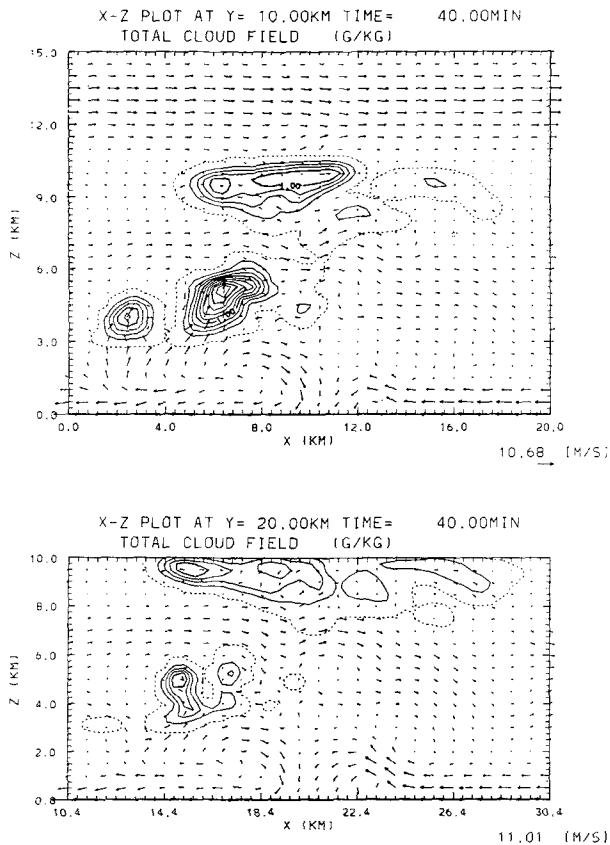X-Z PLOT AT Y= 20.00KM TIME= 40.00MIN
TOTAL CLOUD FIELD (G/KG)

Fig. 17. West-east cross sections of total cloud field for cases FM (a) and MB (b). The contour interval is $0.25\,\mathrm{g\,kg^{-1}}$

west-east vertical cross sections of the total cloud field at equivalent y planes and at time 40–1650 for cases MB and FM. The differences near the west boundary are obvious. The cloud cell near the west boundary in case FM is much stronger than the one in case MB. Looking at the wind vectors in Fig. 17, we see that this secondary cloud cell in case FM is associated with a fairly strong and erect updraft; this cell is much weaker in case MB and the wind vectors only give a hint to the presence of an updraft. The lower portion of the main cloud cell just to the right of the secondary cell is also considerably stronger in case FM. Because the main difference between the FM and MB cases is the location of the artificial lateral boundaries, we can conclude that the stronger updraft near the boundary in case FM is mainly the result of the numerical treatment of the boundary conditions and the proximity of these artificial boundaries to the physical phenomena being modeled. As the extra cloud cell near the west boundary is not evident in the observations,

we can also conclude that the grid nesting improved the model performance in this respect.

6. Summary and Conclusions

In this paper, a modified form of Clark's 3D cloud model has been tested in various modes to simulate the life cycle of a small isolated Montana thunderstorm. The 3D cloud model used in this study has been developed by Clark and associates. Recently, Farley has modified this 3D model to use the bulk water parameterization scheme of Lin et al. (1983), plus secondary ice production and graupel/hail formation via snow (of a certain critical size) accreting supercooled cloud water. This model has been tested under three different grid meshes – coarse mesh CM, fine mesh FM, and one nested model calculation giving fine mesh interactive case MB and coarse mesh interactive case MA (both resulting from the same model run. In the nested grid fine mesh model simulation, the timing and mode of cloud growth, the liquid cloud size, the cloud top rise rate, the maximum cloud water content, and the altitude of first radar echo are consistent with observations. The simulated thunderstorm begins to dissipate after precipitation reaches the ground, as indicated by the decreasing values of maximum updraft and maximum liquid cloud water content, and ends as a precipitating anvil, as was observed in the actual thunderstorm.

The ice phase plays a significant role in the microphysics of this thunderstorm. The model precipitation developed through ice phase processes, which is just like what happened in the actual thunderstorm suggested by the evidence from the observation data analysis. The simulated first radar echo occurred about 7 km MSL due to low density precipitation-sized ice particles which is consistent with observations.

The model-predicted maximum updraft speed of $23.7\,\mathrm{m\,s^{-1}}$ is smaller than the 2D model-predicted maximum updraft speed, but still greater than what was observed. As indicated by Helsdon and Farley (1987), however, the fact that the model-predicted maximum updraft speed is not evident in the observed data does not preclude such a maximum from having occurred in the actual cloud, although it is likely that the simulated maximum was overpredicted by the model. Comparisons with updrafts where the sailplane was, however, were much better.

The qualitative comparison of the simulated and actual radar RHIs for the 3D simulated cloud shows remarkable similarity, especially after the mature stage is reached. Features of the actual RHI patterns, such as the weak echo region, upshear anvil bulge, strong upwind reflectivity gradients, and the upwind outflow region near the surface are reproduced in the simulation. The comparison of the simulated and actual radar PPIs for the 3D simulated cloud, however, shows differences in the storm size. The 3D simulated thunderstorm is somewhat larger than the actual thunderstorm which is well simulated in the 2D model simulation.

The comparison among the 2D, MA, MB, FM, and CM model results shows that the nested grid fine mesh model (MB) gives the best simulation result. The various 3D model simulation results are generally similar to each other despite the difference in the domain maximum values. Domain maximum values for the fine mesh models (MB and FM) are generally higher than for the coarse mesh models as a result of averaging over a smaller area. The grid nesting improved the simulation results, as evident in Table 3.

The most striking deficiency of the 3D simulations has been the overprediction of updraft strength and cloud top height. Additional experiments involving modifications to the initiating bubble and low-level moisture field indicated a relatively weak sensitivity to the character of the bubble, whereas the low-level moisture supply exerted a more pronounced effect. Decreasing the low-level moisture by $0.5\,\mathrm{g\,kg^{-1}}$ to $6.5\,\mathrm{g\,kg^{-1}}$ resulted in a slight lowering of cloud top although the maximum updraft decreased to $16\,\mathrm{ms^{-1}}$, very near the observed maximum. Therefore, for the cases discussed in detail in this study it appears the amount of convective available potential energy (CAPE) is too high.

References

Aleksić, N. M., Farley, R. D., Orville, H. D., 1989: A numerical cloud model study of the Hallett-Mossop ice multiplication process in strong convection. Atmos. Res., 23, 1–30.

Arakawa, A., 1966: Computational design for long term integration of the equations of motion: Two-dimensional incompressible flow. Part I. J. Comput. Phys., 1, 119–143.

Clark, T. L., 1977: A small scale numerical model using a terrain following coordinate system. J. Comput. Phys., 24, 186–215.

Clark, T. L., 1979: Numerical simulations with a three-dimensional cloud model: lateral boundary condition experiments and multi-cellular severe storm simulations. J. Atmos. Sci., 36, 2191–2215.

Clark, T. L., 1982: Cloud modeling in three spatial dimensions, Chapter 10. In: Knight, C. A., Squires, P. (eds.) Hailstorms of the Central High Plains I: The National Hail Research Experiment. Boulder, CO.: Colorado Associated Univ. Press, 282 pp.

Clark, T. L., Farley, R. D., 1984: Severe downslope windstorm calculations in two and three spatial dimensions using anelastic interactive grid nesting: A possible mechanism for gustiness. J. Atmos. Sci., 41, 329–350.

Clark, T. L., Gall, R., 1982: Three-dimensional numerical model simulations of airflow over mountainous terrain: A comparison with observations. Mon. Wea. Rev., 110, 766–791.

Cotton, W. R., Tripoli, G. J., 1978: Cumulus convection in shear flow: three-dimensional numerical experiments. J. Atmos. Sci., 35, 1503–1521.

Dudhia, J., Moncrieff, M. W., 1989: A three-dimensional numerical study of an Oklahoma squall line containing right-flank supercells. J. Atmos. Sci., 46, 3363–3391.

Dye, J. E., Jones, J. J., Winn, W. P., Cerni, T. A., Gardiner, B., Lamb, D., Pitter, R. L., Hallet, J., Saunders, C. P. R., 1986: Early electrification and precipitation development in a small, isolated Montana cumulonimbus. J. Geophys. Res., 91, 1231–1247.

Farley, R. D., Price, P. E., Orville, H. D., Hirsch, J. H., 1989: On the numerical simulation of graupel/hail initiation via the riming of snow in bulk water microphysical cloud models. J. Appl. Meteor., 28, 1128–1131.

Gardiner, B., Lamb, D., Pitter, R. L., Hallett, J., 1985: Measurements of initial potential gradient and particle charges in a Montana summer thunderstorm. J. Geophys. Res., 90, 6079–6086.

Harlow, F. H., Welch, J. E., 1965: Numerical calculation of time-dependent viscous incompressible flow of fluid with free surface. Phys. Fluids, 8, 2182–2189.

Helsdon, J. H., Jr., Farley, R. D., 1987a: A numerical modeling study of a Montana thunderstorm. Part I: Model results versus observations involving non-electrical aspects. J. Geophys. Res., 92, 5645–5659.

Helsdon, J. H., Jr., Farley, R. D., 1987b: A numerical modeling study of a Montana thunderstorm. Part II: Model results vs. observations involving electrical aspects. J. Geophys. Res., 92, 5661–5675.

Jones, J. J., Winn, W. P., Dye, J. E., 1982: Early electrification in a cumulus. Preprints, Conf. Cloud Physics, Boston, MA, Amer. Meteor. Soc., 562–565.

Kessler, E., 1969: On the distribution and continuity of water substance in atmospheric circulations. *Meteor. Monogr. No. 32*, Amer. Meteor. Soc., 84 pp.

Kurihara, Y., Bender, M. A., 1983: A numerical scheme to treat the open lateral boundary of a limited area model. *Mon. Wea. Rev.,* **111**, 445–454.

Lilly, D. K., 1962: On the numerical simulation of buoyant convection. *Tellus,* **14**, 148–172.

Lilly, D. K., 1965: On the computational stability of numerical solutions of time-dependent nonlinear geophysical fluid dynamics problems. *Mon. Wea. Rev.,* **93**, 11–26.

Lin, Y. L., Farley, R. D., Orville, H. D., 1983: Bulkparameterization of the snow field in a cloud model. *J. Climate Appl. Meteor.,* **22**, 1065–1092.

Miller, M. J., 1978: The Hampstead storm: A numerical simulation of a quasistationary cumulonimbus system. *Quart. J. Roy. Meteor. Soc.,* **104**, 413–427.

Ogura, Y., Phillips, N. A., 1962: Scale analysis of deep and shallow convection in the atmosphere. *J. Atmos. Sci.,* **19**, 173–179.

Orlanski, I., 1976: A simple boundary condition for unbounded hyperbolic flows. *J. Comput. Phys.,* **21**, 251–269.

Orville, H. D., 1985: Comment on "Effects of the pressure perturbation field in numerical models of unidirectionally sheared thunderstorm convection: two versus three dimensions." *J. Atmos. Sci.,* **42**, 2220–2221.

Orville, H. D., Kopp, F. J., 1977: Numerical simulation of the history of a hailstorm. *J. Atmos. Sci.,* **34**, 1596–1618.

Redelsperger, J. L., Lafore, J. P., 1988: A three-dimensional simulation of a tropical squall line: Convective organization and thermodynamic vertical transport. *J. Atmos. Sci.,* **45**, 1334–1356.

Schlesinger, R. E., 1978: A three-dimensional numerical model of an isolated thunderstorm: Part I. Comparative experiments for variable ambient wind shear. *J. Atmos. Sci.,* **35**, 690–713.

Schlesinger, R. E., 1984: Effects of the pressure perturbation field in numerical models of unidirectionally sheared thunderstorm convection: two versus three dimensions. *J. Atmos. Sci.,* **41**, 1571–1587.

Smagorinsky, J., 1963: General circulation experiments with the primitive equations: I. The basic experiment. *Mon. Wea. Rev.,* **91**, 99–164.

Smith, P. L., Jr., Myers, C. G., Orville, H. D., 1975: Radar reflectivity factor calculations in numerical cloud models using bulk parameterizations of precipitation. *J. Appl. Meteor.,* **14**, 1156–1165.

Smolarkiewicz, P. K., 1984: A full multidimensional positive definite advection transport algorithm with small implicit difussion. *J. Comput. Phys.,* **65**, 325–363.

Smolarkiewicz, P. K., Clark, T. L., 1985: Numerical simulations of the evolution of a three-dimensional field of cumulus clouds. Part I: Model description, comparison with observations and sensitivity studies. *J. Atmos. Sci.,* **42**, 502–522.

Smolarkiewicz, P. K., Clark, T. L., 1986: The multinational positive definite advection transport algorithm. Further development and applications. *J. Comput. Phys.,* **67**, 394–439.

Steiner, J. T., 1973: A three-dimensional model of cumulus cloud development. *J. Atmos. Sci.,* **30**, 414–435.

Wang, S., 1989: A comparison of 3D and 2D cloud model results with observations and among themselves. M.S. Thesis, Dept. of Meteorology, S. D. School of Mines and Technology, Rapid City, SD, 94 pp.

Wisner, C., Orville, H. D., Myers, C., 1972: A numerical model of a hail-bearing cloud. *J Atmos. Sci.,* **29**, 1160–1181.

WMO, 1986: Weather modification research programme, Irsee, FRG. WMP No. 8, Report of the Intnl. Cloud Modeling Workshop/Conf., Tech. Document WMO/TD-No. 139, Geneva.

WMO, 1988: Cloud physical and weather modification research programme, Toulouse, France. WMP No. 11, Report of the Second Intnl. Cloud Modeling Workshop/Conf., Tech. Document WMO/TD-No. 268, Geneva.

Authors' addresses: R. D. Farley, S. Wang and H. D. Orville, Institute of Atmospheric Sciences, South Dakota School of Mines and Technology, 501 E. St. Joseph Street, Rapid City, South Dakota 57701 3995, U.S.A.